

# ON OBSERVING THE COSMIC MICROWAVE BACKGROUND

L.A. PAGE  
*Princeton University*  
*Dept. of Physics*  
*Princeton, NJ*

## **Abstract.**

The cosmic microwave background (CMB) comprises the oldest photons in the universe and is arguably our most direct cosmological observable. All precise and accurate measurements of its attributes serve to distinguish between cosmological models. Detector technology and observing techniques have advanced to the point where fluctuations in the CMB of order a few microkelvin are measured almost routinely. In these lecture notes, we review recent measurements of both the absolute temperature and the anisotropy of the CMB and discuss the relation between the data and the general theoretical framework. Future directions are indicated and the upcoming satellite experiments are discussed.

## **1. Introduction**

The CMB is a powerful probe of cosmology because essentially no steps separate what is measured from what is of cosmological import; what you see is what you get. The CMB photons have free-streamed through the cosmos since last scattering off electrons some 100,000 years after the big bang. The spectrum of the CMB is indistinguishable from a Planck function to roughly 0.01% accuracy. This tells us that there were not any highly energetic cosmic processes, that coupled to photons, before  $z \approx 10^3$ . The near perfect shape of the spectrum is the strongest evidence to date that the hot big-bang model is correct. The pattern of minute spatial variations or anisotropy in the CMB, which are of order  $\delta T/T \approx 10^{-5}$ , is a fossil of the early universe. Furthermore, most models that give rise to cosmic structure affect the CMB, leaving an imprint of a small temperature fluctuation.

There are many review articles on both the spectrum of and anisotropy in the CMB. For the anisotropy see [1]-[6]; for a recent review of both the spectrum and anisotropy results see [7] and [8]; and for reviews of the theory and results on the spectrum see [9], [10], or [11]. In addition, Partridge has written a new book [12] devoted to the subject.

The outline for these notes is as follows. We discuss the microwave/far-infrared sky in Section 2. Next, in Section 3, we discuss the recent results of absolute temperature measurements of the CMB. After a model of the anisotropy is developed in Section 4, Section 5 provides a discussion of the measurement technologies and an overview of the canonical formalism for describing the anisotropy. In Section 6, we review the state of the field. We end with a discussion of the upcoming satellite missions in Section 7.

## 2. The Microwave/Far-Infrared Sky

The CMB is the brightest broad-band diffuse emitter in the sky between about 1 and 500 GHz, completely dominating the Galactic foreground emission. At the low frequency end of this range, Galactic synchrotron emission exceeds the CMB and at the high frequency end, interstellar dust emission dominates. Galactic bremsstrahlung, or free-free emission, is the largest foreground near 90 GHz. Figure 1 shows the frequency spectrum of the diffuse Galactic emission between 3 and 3000 GHz near a Galactic latitude of  $20^\circ$ . There are two sources not shown on this plot. Near 3000 GHz, thermal emission from the interplanetary dust (Zodiacal light) is roughly ten times smaller than the interstellar dust and its brightness scales with frequency as  $\nu^4$ . Throughout the plotted range, interstellar molecular line emission is also observed [13].

In addition to the diffuse foreground, galactic and extragalactic point-like objects such as quasars, blazars, gigahertz-peaked sources, and loud radio sources also emit microwave and far-infrared radiation. The spectrum of most sources falls with increasing frequency, though not of every source.<sup>1</sup> Relatively little is known about sources near 90 GHz. There are no deep unbiased surveys from which to ascertain the ensemble properties with confidence. Also, we know that many of the extragalactic high-frequency sources are variable.

In Figure 1 it is evident that to probe either the spectrum or the anisotropy to a part in  $10^3$  or  $10^5$  the foreground emission must be confronted. Before COBE[14], the best full-sky maps were the ‘‘Haslam *et al.*’’ map at 408 MHz[15] and the IRAS dust map, with Zodiacal light subtracted, at 3000 GHz (100  $\mu\text{m}$ )[16]. Extrapolation of these maps to fre-

<sup>1</sup>For sources, ‘‘flat spectrum’’ means that  $S(\nu)$  is independent of  $\nu$ , similar to free-free emission.

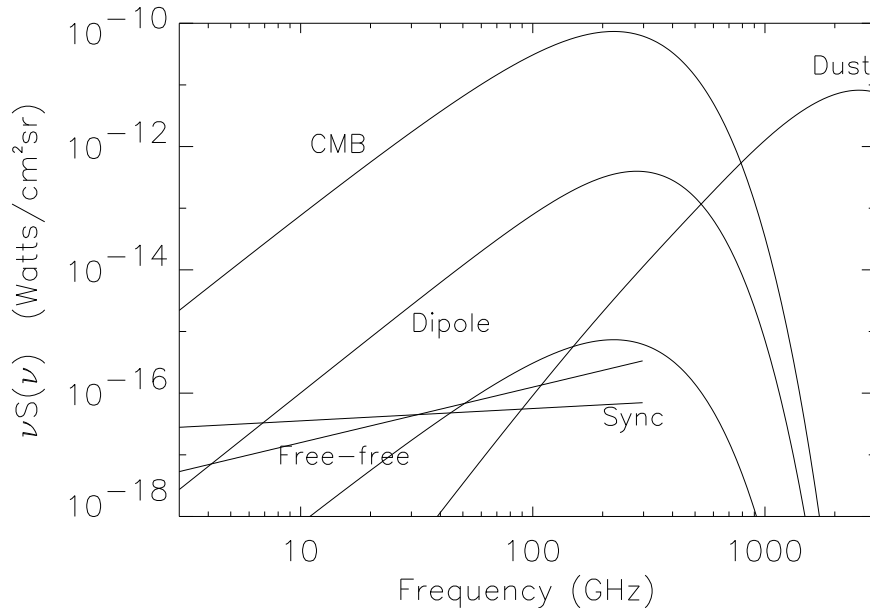


**Figure 1.** The microwave sky from 3 to 3000 GHz near a Galactic latitude of  $b = 20^\circ$ . The ordinate is the brightness of the sky times the frequency. With this convention, the plot indicates the distribution of power. For synchrotron emission  $S(\nu) \propto \nu^{-0.7}$ ; for free-free emission  $S(\nu) \propto \nu^{-0.1}$ ; and for dust emission near 100 GHz  $S(\nu) \propto \nu^{3.7}$ . The scaling in effective temperature is  $T(\nu) \propto \nu^{-2}S(\nu)$ . The lowest Planck-like curve is for  $T = 27 \mu\text{K}$ .

requencies of interest is problematic because the spectral index varies from place to place on the sky and there are components, such as free-free and cold dust emission, that are missing from these maps. A believable CMB spectrum or anisotropy experiment *must* measure the CMB and foreground emission to similar precision.

In addition to the frequency dependence of the foreground emission, there is also a spatial dependence. At the largest angular scales, Galactic emission falls off with Galactic latitude roughly as  $1/\sin(b)$ . In other words, its intensity distribution, to first order, resembles a quadrupole: hot around a circle, cold near the poles. Indeed this quadrupole confounded some of the early measurements of the anisotropy and its removal from the *COBE/DMR* data requires ingenuity [17].

The spatial distribution of celestial sources is commonly quantified with

the angular spectrum. This formalism is used to describe the anisotropy, radio sources, and the diffuse foreground. It allows a direct comparison of the contribution from each. To illustrate it, the relatively simple case of foreground emission by extra-galactic radio sources is considered. We assume radio sources are randomly placed on the sky and so the angular spectrum should be that of “white noise.” If we measure the total source emission temperature in each sky pixel, then that distribution may be represented as an expansion in spherical harmonics,

$$T(\hat{x}) = \sum_{l,m} a_{lm} Y_{lm}(\hat{x}), \quad (1)$$

where  $\hat{x}$  is the unit vector in some direction. At this time we will ignore the effects of finite measurement resolution; this will be considered later. The correlation function (or two-point function) of the temperatures is defined as

$$C(\theta) = \langle T(\hat{x})T(\hat{y}) \rangle, \quad \text{where } \theta = \hat{x} \cdot \hat{y}, \quad (2)$$

and where the diagonal bracket indicates an ensemble average over many universes. For small angular scales, the ensemble average can be replaced by an average over positions in our universe. For a Gaussian random field, all the information is contained in the two-point correlation function (eq. 2). We do not know if the CMB is a Gaussian field, and we know that Galactic emission is certainly not. However, we still use the two-point function; a more complete description would use the higher-point correlation functions. Because  $C(\theta)$  depends only on the angular separation between two directions, it may be expanded in Legendre polynomials as

$$C(\theta) = \sum_l \frac{2l+1}{4\pi} C_l P_l(\cos(\theta)) \quad \text{where } C_l = \langle |a_{lm}|^2 \rangle. \quad (3)$$

Here the brackets denote averaging over the  $2l+1$  values of  $m$ . The variance of the pixel temperatures is given by  $C(0)$ . Because  $P_l(0) = 1$ , the variance in each “mode”  $l$  is just  $(2l+1)C_l/4\pi$ . For “white noise,”  $C_l = \text{const}$ . We may see this by considering that the magnitude squared of the Fourier transform of a uniform distribution of sources will also be a uniform distribution in 2-D Fourier space; there is no preferred scale. Call the uniform value  $U$ . For small angles, the conjugate variable to angular separation is  $l+1/2$ , where  $l+1/2 \approx l = 1/\delta\theta$  where  $\delta\theta$  is the angular scale. Now, the variance for a band of modes of width  $\delta l$  at a radius  $l$  is given by the area in Fourier space or  $U2\pi l\delta l$ . In other words, the  $C_l \propto U = \text{const}$ .

To visualize the angular spectrum (“power spectrum” is usually reserved for the  $C_l$ ), one generally plots  $(l(2l+1)C_l/4\pi)^{1/2} = \delta T_l$  versus  $l$ . The

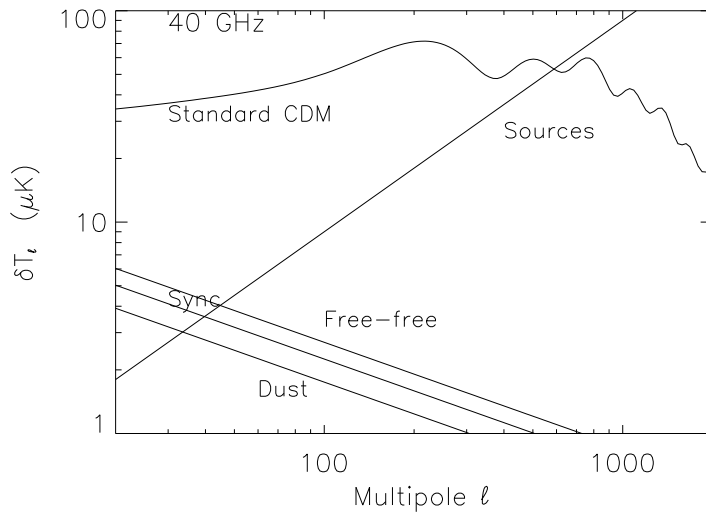


**Figure 2.** Spatial spectrum of the foregrounds from Netterfield *et al.* [18] and references therein. This is for the region near the North Celestial Pole at a frequency of 40 GHz. At higher frequencies, the flux from dust increases and that from synchrotron and radio sources decreases. The curved line is for standard CDM (from [19]).

extra factor of  $l$  means that  $\delta T_l$  is the root mean squared fluctuation per logarithmic interval,  $\delta l/l$ . The results from such an analysis for radio sources and Galactic emission at 40 GHz are shown in Figure 2.

From Figures 1 and 2, it is clear that the foreground emission must be well understood before the absolute CMB spectrum is known to 0.01% near 3 GHz or before the angular spectrum is known to the few percent level. One mitigating factor for the anisotropy is that the foreground fluctuations add to the signal in quadrature in the approximation that they are random fields. The absolute measurements do not enjoy this benefit. We are a long way from understanding the Galactic emission and radio sources. For a thorough up-to-date assessment, see Tegmark and Efstathiou [20].

### 3. Measurements of the Spectrum

The spectrum of the CMB is as close to that of a blackbody as can be measured; no distortions have been detected. This is our best evidence that the universe went through a hot dense phase when everything that interacts with photons was in thermal equilibrium. In current models, the epoch of

photon production ended at  $z \approx 3 \times 10^6$ , when the universe was roughly two months old. In the subsequent expansion, an injection of energy mediated by baryons would distort the spectrum, though the injection would have to be large (or efficient) to be detectable today because there are roughly  $10^9$  photons per baryon. Thus a study of the spectrum is a study of the history of cosmic energetics.

The FIRAS experiment [21] aboard the *COBE* [14] satellite measured the flux from the sky between 2 and 96  $\text{cm}^{-1}$  (60 – 2880 GHz). Fixsen and colleagues give the most recent results [22] and discuss the exhaustive program of systematic checks and instrument calibration [23]. The FIRAS team finds that the flux is described by the Planck function with a temperature of

$$T_{\text{CMB}} = 2.728 \pm 0.004 \text{ K.} \quad (4)$$

One doubts that short of another satellite-based experiment this result will be matched or bettered at frequencies above 100 GHz. It is comforting that the UBC rocket experiment [24] gives a consistent result.

The error on the FIRAS result, 4 mK, is due entirely to systematic effects and Fixsen *et al.* interpret it as a 95% confidence limit. (The statistical error is 7  $\mu\text{K}$ .) The error exists to tell the readers how confident the authors are in the results. It should not be interpreted in the sense that “if one hundred experiments were performed only ten would lie outside the error bounds.”

When interpreting this result, one must bear in mind that it comes from a *model* of the data. If the model is not correct, the results must be re-interpreted. To be more specific, the analyzed data come from maps of the sky in multiple frequency bands between 2 and 21  $\text{cm}^{-1}$ . A four parameter fit is made to the maps at  $|b| > 5^\circ$  at each frequency,

$$\text{FIRAS}(\nu) = \alpha_0(\nu)\text{Uniform} + \alpha_1(\nu)\text{Dipole} + \alpha_2(\nu)\text{D9} + \alpha_3(\nu)\text{D10.} \quad (5)$$

The fit parameters scale the spatial distributions of a uniform background, the CMB dipole, channel 9 from the DIRBE experiment (D9, 72  $\text{cm}^{-1}$ ) and channel 10 from the DIRBE experiment (D10, 42  $\text{cm}^{-1}$ ). The last two maps are found to be good measures of the interstellar dust distribution. Two maps are needed because there may be multiple dust components or, in an explanation that Fixsen [25] prefers, the dust temperature may be a function of position.

The set of coefficients of the uniform component,  $\alpha_0(\nu)$ , is then fit to a combination of four frequency distributions. They are a) a blackbody, b) the derivative of a blackbody (to fit an error to the temperature scale), c) the

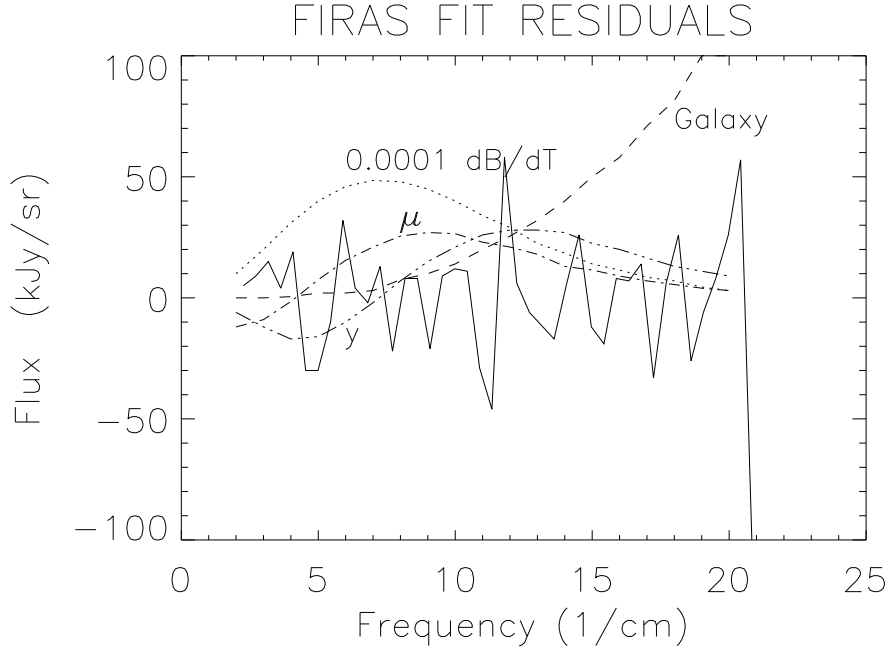


**Figure 3.** Residuals of the fit to  $\alpha_0(\nu)$  in eq. 5 from [22]. If one starts with the  $\alpha_0(\nu)$  in eq. 5 and subtracts a blackbody (curve not shown), a small calibration correction term ( $0.0001 \text{ dB/dT}$ , where  $B(\nu)$  is the Planck function), and a model of the Galactic spectrum, the solid line is obtained. The Galactic spectrum is shown scaled to 1/4 its value at the galactic poles. In other words, if a Galactic-type spectrum were not subtracted, the spectrum of the uniform sky map would rise with frequency. The peak of the CMB is near  $\nu = 5.5 \text{ cm}^{-1} = 165 \text{ GHz}$ . The intensity measured there is roughly  $385 \text{ MJy/sr}$ . The  $\mu$  and  $y$  distortions are shown at the 95% CL values in eq. 6. The units on the abscissa are converted to GHz by multiplying by 30.

spectrum of the Galaxy (that accounts for residual Galactic signal in the monopole!), and d) a spectral distortion. The distortion is parameterized by either a chemical potential  $\mu$ , or a Compton  $y$ -factor. Only one distortion is fit at a time because the spectral signatures of the two are anti-correlated. The residuals to this fit and some of the basis functions are shown in Figure 3.

Before  $z \approx 3 \times 10^6$ , double Compton scattering and free-free emission maintain the thermal equilibrium of the CMB with the surroundings by

creating photons. An energy input simply results in a hotter CMB temperature. Between  $10^5 < z < 3 \times 10^6$ , single Compton scattering, which conserves the number of photons, is the dominant scattering mechanism over most of the frequency spectrum. In this epoch, the CMB is in *statistical* equilibrium with its surroundings and the distribution is characterized by a chemical potential  $\mu$ . (The quoted numbers are for the unitless chemical potential; the flux is  $S_\nu(T, \mu) = 2h\nu^3/[\exp(h\nu/kT_{CMB} + \mu) - 1]$ ). At long wavelengths, free-free emission is still effective and “fills in the tail” of the distribution. For  $z < 10^5$ , hot electrons, which are neither in statistical nor in thermal equilibrium with the CMB, can inverse Compton scatter the CMB photons to produce a Compton  $y$  distortion. When there are relatively few scattering events, one may think of  $y$  as the average fractional energy change per scattering event times the average number of scatterings [26], or  $y = 1/m_e c^2 \int [k(T_e - T_{CMB})] d\tau_e$  [9] where  $T_e$  is the electron temperature and  $\tau_e$  is the optical depth due to scattering. Finally, if the universe is ionized at  $z < 10^3$  then there may be enough free-free emission from the plasma to increase the photon occupation number at large  $\lambda$  and thus the temperature there. This distortion is parameterized by  $Y_{ff} = (h\nu/kT)^2 [T_{eff}(\nu) - T_{CMB}]/T_{CMB}$ , with  $T_{eff}$  the plasma temperature. These and other distortions, along with their interpretation, are discussed in [9], [11], [27], [4].

The best limits on  $y$  and  $\mu$  come from FIRAS [22]. From these, Wright *et al.* [27] constrain energy injection in the early universe as shown in Figure 4. The limit on  $Y_{ff}$  [28] comes from a fit of the low frequency data. The limits are:

$$\begin{aligned} |y| &< 1.5 \times 10^{-5} \quad 95\% \quad CL, \\ |\mu| &< 9 \times 10^{-5} \quad 95\% \quad CL, \\ Y_{ff} &< 1.9 \times 10^{-5} \quad 95\% \quad CL. \end{aligned} \tag{6}$$

The  $y$  distortion is manifest at high frequencies and it will be a long time before the FIRAS limit is improved. The limit on  $y$  also strongly constrains alternative models of the origin of the CMB. One may try to mimic a Planck spectrum with a superposition of multiple grey bodies. At long wavelengths, the Rayleigh-Jeans region, the results cannot be distinguished. However, near the peak of the spectrum, such a superposition will result in a  $y$ -distortion. We also note that if the universe is inhomogeneous on the largest scales, and we are not at a preferred center, a distortion will result [29].

The signatures of any  $\mu$  and  $Y_{ff}$  distortions are evident at low frequencies. While the current generation of experiments will just barely, if at all, improve on the FIRAS limits, they are paving the way for the next genera-



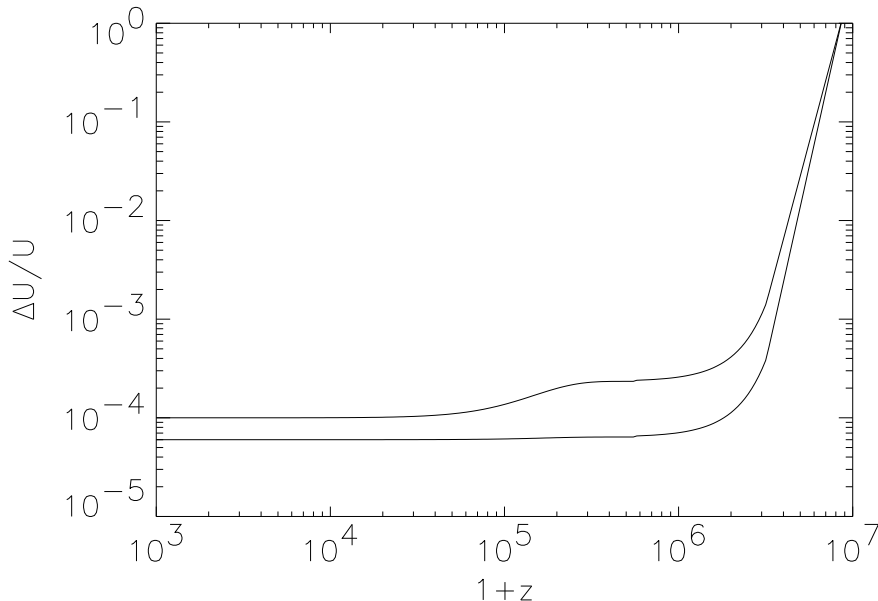


**Figure 4.** Limits on energy injection into the CMB prior to decoupling. The top curve uses  $y = 2.5 \times 10^{-5}$  and  $\mu = 3.3 \times 10^{-4}$ . These were the limits from FIRAS in 1994 (Wright *et al.* [27]). The different epochs are clearly evident. The bottom curve is based on the FIRAS limits in eq. 6. This plot was produced with a program written by Ned Wright and is based on models in Burigana *et al.* [32], [33].

tion which may detect a distortion. Figure 5 shows a plot of the spectrum along with the  $\mu$  and  $Y_{ff}$  distortion limits.

Two groups [30], [31] are pursuing long-wavelength measurements of the spectrum. Outside of the precise instrumentation necessary to perform absolute measurements between 0.1% and 1%, one must contend with Galactic and atmospheric emission. At 600 MHz, the temperature of the Galaxy is roughly 5.8 K [34] and falls as  $\nu^{-2.7}$ . In Figure 1, this is roughly where the “synchrotron” and “CMB” lines cross. Observing from the ground, the atmosphere emits at roughly 1.5 K between 0.6 GHz and 1.4 GHz [34], [35]. Ground-based experiments thus require precise modeling and sky dips to subtract the atmospheric signal. Compact experiments may be flown from balloons to rise above it. Finally, in the not-too-distant future, narrow-band measurements will be limited by the FIRAS error when characterizing distortions.

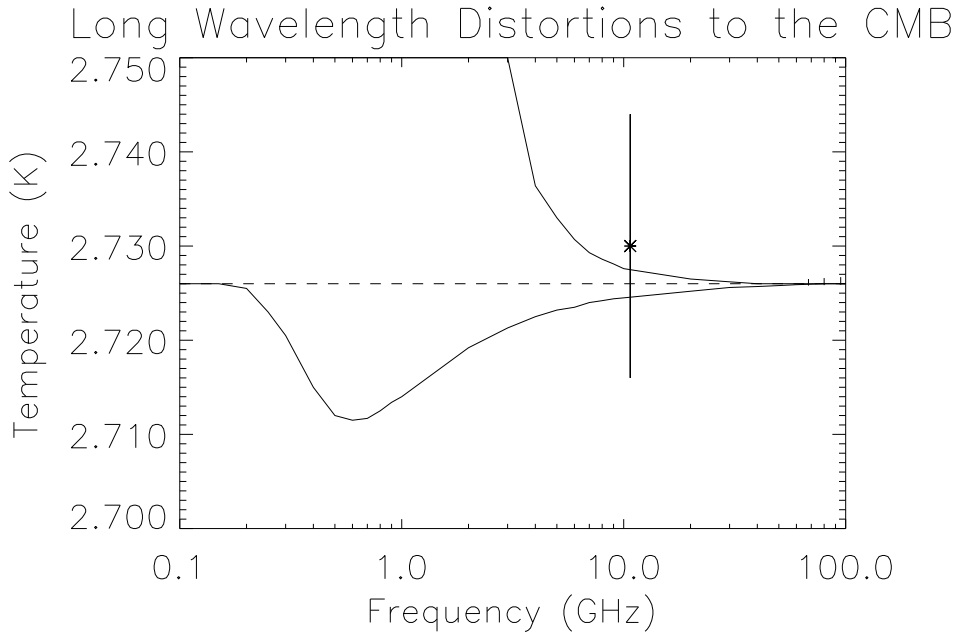


**Figure 5.** Plot of the long wavelength (low frequency) distortions to the CMB. The flat line is for a perfect blackbody. The curve with a pronounced minimum near 700 MHz shows a  $\mu$  distortion with  $\mu = 9 \times 10^{-5}$ , the *COBE* limit. The curve that begins to rise near 10 GHz is for a  $Y_{ff}$  distortion with  $Y_{ff} = 1.5 \times 10^{-5}$ . All data with error bars small enough to fit on this plot are shown. The measurement at 10.7 GHz comes from Staggs *et al.* [30]. Note the three FIRAS data points near 100 GHz. This plot was adapted from a similar plot made by Al Kogut.

#### 4. The Anisotropy

The photons that end their lives in our detectors were last scattered off electrons when the universe had a temperature of 5000 K and was evolving from a plasma to a state of neutral hydrogen and helium plus a thermal background<sup>2</sup>. This era is called the epoch of decoupling. The plasma was responding to the gravitational potential wells that would eventually foster galaxies and clusters of galaxies. The photons, now decoupled, bring to us an imprint of the potential wells and a signature of the dynamics of the

<sup>2</sup>We assume the standard inflationary model in this discussion, as well as a nearly complete transition from plasma to neutral matter.

plasma’s response to the wells. From the angular spectrum of the fluctuations, one can distinguish among various possible mechanisms of structure formation. In recent years, it has become evident that for a certain class of models (eg. standard CDM<sup>3</sup>), a measurement of the detailed shape of the power spectrum will yield values for many of the cosmological parameters<sup>4</sup> such as  $\Omega_0$ ,  $\Omega_B$ ,  $H_0$ , and  $\Lambda$  [36].

Figure 6 shows the angular spectra for a few of the many models of structure formation. The point of the plot is to indicate that the model predictions are rather different and that given measurements with uncertainties of order the width of the plot line, the best model could be identified.

We divide the spectrum into three regions. At  $l < 80$ , or large angular scales ( $\delta\theta > 2^\circ$ ,  $l \approx 180/\delta\theta$  with  $\delta\theta$  in degrees), separate regions of the sky are not causally connected at decoupling. Indeed, the relative isotropy at these scales was one of the motivations for the inflation model. If inflation is correct, these potential wells and hills are the manifestation of quantum fluctuations that were superluminally expanded beyond the Hubble radius, grew with the expansion of the universe, and then re-entered the Hubble radius at a later time. The largest scales entered the Hubble radius most recently. In 10 billion years, a new CMB quadrupole will come into view as the universe expands and what we now call the quadrupole will be distributed among the higher moments. At these large scales, the anisotropy is produced by photons climbing out of the gravitational potential wells or sliding down the hills, just after their last scattering event, as discovered by Sachs and Wolfe. The anisotropy in this region reflects the primordial power spectrum of fluctuations,  $P(k)$ . One of the strengths of inflation is that it predicts the shape of this spectrum<sup>5</sup>. At large angular scales,  $C_l \propto 1/l(l+1)$ , in other words, a nearly flat line in Figure 6.

At smaller angular scales, greater than  $l \approx 80$ , there was time for the primordial plasma to communicate. Hu and colleagues [6], [5] have presented an intuitive physical picture of the mechanisms behind the anisotropy although models date back to Silk [39], Sunyaev and Zel’dovich [40], Peebles & Yu [41] and others. To first order, we may think of the plasma as a photon-baryon fluid that acoustically oscillates in response to fluctuations in the gravitational potential produced by the dark matter. As the fluid flows into a potential well, it heats up (the phase is opposite to that of

<sup>3</sup>Standard CDM has  $\Omega_0 = 1$ ,  $h = 0.5$ ,  $\Omega_B = 0.05$ , and  $n = 1$ . Ratra points out that “fiducial” is a better description because many observations disagree with standard CDM.

<sup>4</sup> $\Omega$  is the fraction of the critical density. For standard Cold Dark Matter models,  $\Omega_0 = \Omega_{CDM} + \Omega_B$ ; for Lambda models,  $\Omega_0 + \Omega_\Lambda = 1$ ; while for open models,  $\Omega_0 + \Omega_\Lambda + \Omega_{curv} = 1$ .

<sup>5</sup>The shape of the spectrum was surmised independently by Harrison, Peebles & Yu, and Zel’dovich long before inflation.

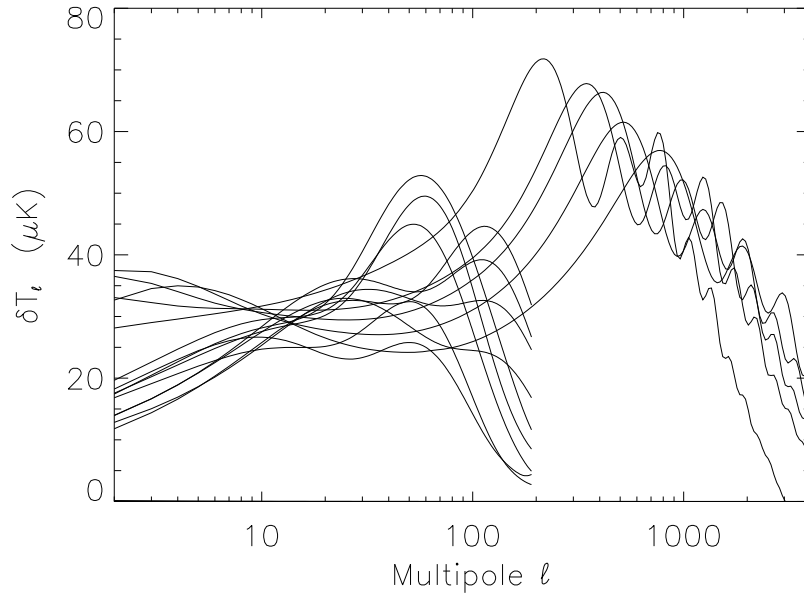


**Figure 6.** Angular spectrum for a sample of anisotropy models. The curves grouped on the left hand side are the predictions of isocurvature models from Peebles [37]. The curves that peak on the right are for the standard and open bubble inflation models (Ratra and Sugiyama [38], [19]) with  $\Omega_0 = 1.0, 0.4, 0.3, 0.2$  and  $0.1$  for peaks going from left to right.

the Sachs-Wolfe effect). This is responsible for the large peak in the power spectrum which occurs at roughly the angular scale of the largest potential that can support plasma oscillations. Oscillations of the fluid in response to fluctuations at smaller scales give rise to the other peaks. A full description accounts for the doppler effect, the self gravity of the photon-baryon fluid, the inertia of the baryons, and the evolution of the fluid with time.

Because decoupling happened so fast,  $\delta z/z \approx 0.1$ , the thickness of the surface of last scattering is less than the horizon size at  $z \approx 1400$ . The scale of the fluctuations near the first peak is of order the horizon size, about 100 Mpc in comoving units<sup>6</sup>, and we observe the full signature of the potential wells there. On smaller angular scales, corresponding to smaller physical scales, there are more fluctuations contained within the horizon and their

<sup>6</sup>Alex Szalay spoke of a possible connection between this scale and the scale of the largest structure in the galaxy surveys.

effects average out. In addition, diffusion of photons out of the potential wells diminishes the temperature fluctuations. The combination of these effects leads to the suppressed anisotropy near  $l = 2000$  as can be seen in Figure 6.

Cosmological parameters are extracted from the shape of the power spectrum. For standard CDM type models this is done, for instance, by noting that the distance between the peaks depends on the sound speed at decoupling. This in turn depends on  $h^2\Omega_B$ . Also, as  $\Omega_B$  increases, the photon-baryon fluid has more inertia (the sound speed decreases) and the compressional peaks (the odd ones starting at  $l = 200$ ) get bigger. On the other hand, if the universe goes through a period of reionization, all the peaks in the anisotropy can be wiped out. Extracting generic cosmological information, regardless of model, is an active area of research [42].

One particularly nice demonstration of what the anisotropy can tell us was noted by Kamionkowski *et al.* [43]. The location in  $l$  of the first peak is a good indicator of  $\Omega_0 + \Omega_{\Lambda}$ . This happens because a universe of any geometry, in its early stages, evolves as though  $\Omega_0 = 1$ . Because the physical size of a fluctuation depends on the sound horizon at decoupling, it is a “standard yardstick.” The angular size of the standard yardstick, as viewed today, depends on the overall geometry of the universe. If the universe is flat, it will appear at  $2^\circ$ , if it is open it will appear at a smaller angle; this last is because there is “more space” far away. This effect is seen in the CDM models in Figure 6. The lower  $\Omega_0$ , the further to the right the peak moves. The scaling is roughly  $l_{peak} \approx 200/\Omega_0^{1/2}$ .

In models of the formation of large scale structure, the same potential fluctuations that produce the anisotropy also produce the large scale clustering of galaxies. We still do not know what type of mass comprises galaxies, or how it couples to gravitational fluctuations, or even what produced the fluctuations. In the past few years, a number of large galaxy surveys have been undertaken and older surveys have been re-analyzed. Over a region of  $l$ -space between  $l = 30$  and  $l = 600$ , there is overlap between the two probes of the fluctuations: galactic surveys and CMB anisotropy data. There is a nice plot of this in White, Scott, & Silk’s review [3]. Unfortunately, the data are not sufficiently good, from either probe, to draw firm conclusions. However, the indications are that the simplest models for the formation of structure are incorrect.

## 5. Anisotropy Measurements: Technologies & Techniques

### 5.1. TECHNOLOGIES

The desire to characterize the anisotropy has led to improvements in detectors and instrument technology. For the anisotropy, three classes of detec-

tor are now in use: HEMT based amplifiers (20-90 GHz), superconductor-insulator-superconductor (SIS) based mixers (90-250 GHz), and a variety of types of bolometers (90-1000 GHz). Anisotropy measurements require very stable observing conditions. This is especially true for “configuration-space” measurements, as opposed to interferometric measurements. To overcome atmospheric fluctuations, the primary culprit, experiments are performed at stable or high sites (Mauna Kea, South Pole, Owens Valley, Saskatoon, & Tenerife) and from balloon platforms. Plans are underway for long duration balloon flights that circumnavigate the Antarctic and for balloons that can stay aloft for 100 days. Interferometers, which currently operate mostly below 30 GHz, are intrinsically less sensitive to the atmosphere.

The HEMT amplifiers for most of the HEMT-based experiments were designed by Marian Pospieszalski at the National Radio Astronomy Observatory (NRAO) electronic research lab. One couples celestial radiation to the amplifiers with waveguide. The incident electric field is simply amplified to a reasonable level and then detected with a diode. The amplifiers are special because they are rugged, require only modest cooling ( $\approx 20$  K), and have a 30% bandwidth. A good wide-band (10 GHz) sensitivity for an optimized system near 40 GHz is roughly  $500 \mu\text{Ks}^{1/2}$ . In other words, one can detect 1/2 mK signal with a signal-to-noise of one with one second of integration. A number of semi-conductor groups are pushing to make better high-frequency transistors (for instance TRW and Hughes) and to make entire radiometers on a single chip (TRW and Lockheed-Martin).

SIS-based systems have been used for a number of years (Timbie [44], Meinhold [45], Robertson [46]) though the anisotropy has not yet been detected with them. The currently favored designs, and devices, come from Anthony Kerr and S-K Pan at NRAO. The SIS is a mixer. It is simultaneously illuminated with celestial radiation and with a “local oscillator.” The output of the SIS is a signal containing the sum and difference frequencies of the LO and sky. The signal is low-pass filtered, amplified with HEMTs, and detected. For a system with a LO at 144 GHz and a 4 GHz IF bandwidth, a reasonable sensitivity is  $400 \mu\text{Ks}^{1/2}$ . These devices must operate below the superconducting transition of niobium, or below roughly 4.2 K. They are more difficult than HEMTs to operate but are still straightforward.

Both HEMT and SIS systems are coherent; in other words, one works with the electric field right up until the final detection. This allows possibilities for phase sensitive techniques such as correlation receivers and interferometers. In addition they both have a very large audio bandwidth. Signals at many megahertz are easily detected.

The current bolometers are essentially thermistors held at 0.3 K or below. When they are illuminated, they heat up and change resistance, and the change in resistance is electronically read out. This is called incoher-

ent detection because the phase information is lost. The great advantage to bolometers is that they are very sensitive. A decade ago, they were near  $400 \mu\text{Ks}^{1/2}$  [47], and some current devices (the “spider” bolometers, Bock et al. [48]) achieve better than  $100 \mu\text{Ks}^{1/2}$ . The disadvantage is that they are more difficult to use than HEMTs and SISs and their intrinsic time constants are longer, but both of these problems are actively being worked on. There are different types of bolometers in various stages of development. They include frequency sensitive bolometers[49], hot electron bolometers[50], monolithic silicon bolometers[51], spider web composite bolometers[48], and transition edge bolometers[52].

The bolometer’s advantage is not its intrinsic sensitivity per photon, which is comparable to that of HEMTs or SIS, but rather the fact that one can detect in multiple electromagnetic modes (in conventional use, waveguide supports just one mode) and almost arbitrary bandwidth. In other words, bolometers detect more photons than single mode waveguide systems. The power on a device is

$$P = \int_{\nu} \int_A \int_{\Omega} S_{\nu}(T) d\nu dA d\Omega \rightarrow \int_{\nu} kT(\nu) d\nu \quad \text{Watts}, \quad (7)$$

where  $S_{\nu}(T)$  is the flux from some source,  $\nu$  is the RF frequency,  $A$  is the area of the detector (or antenna), and  $\Omega$  is the solid angle incident on that detector (or antenna). The quantity  $\int dA d\Omega$  is called the throughput or étendue. Generally,  $A\Omega = n\lambda^2$  where  $\lambda$  is the wavelength at the passband center and  $n$  is the number of modes. For a single mode system,  $n = 1$ , and we get the quantity on the right of the arrow, where  $T(\nu)$  is the effective temperature of the source.

## 5.2. TECHNIQUES

The experimental challenge is to measure a variance of a random field, which is of order  $30 \mu\text{K}$ , with a noisy detector and a background signal of  $300 \text{ K}$ . As much effort has gone into determining robust ways to do this as has gone into understanding the detector systems. The configuration-space techniques are the better developed so we will focus on those. The interferometric techniques are rapidly maturing and have a lot of promise; the first detection of the anisotropy with an interferometer was just reported in Scott *et al.* [53].

A typical telescope has a beam described by  $P(\theta) \propto \exp(-\theta^2/2\sigma^2)$ . If the telescope observes the sky which has temperature  $T(\hat{x})$ , it measures  $t(\hat{x}) = \int P(\theta)T(\hat{x})dx$ . If two measurements made near each other,  $t(\hat{x}_1)$  and  $t(\hat{x}_2)$  are subtracted, the common atmospheric signal drops out. One is then sensitive to only the gradient in the atmosphere and to the CMB temperature difference. If two single differences, with one position

in common, are performed and then subtracted the “double difference” is  $s_i = 2t(\hat{x}_1) - t(\hat{x}_2) - t(\hat{x}_3)$ . The double difference is still sensitive to the CMB but is insensitive to atmospheric gradients as well as the atmospheric temperature. This extra difference helps because the fluctuation spectrum of the atmosphere drops with both increasing spatial and spectral frequency. Let us call the effective beam profile for the double difference measurement  $H_i(\hat{x})$ ; it will have one large positive central lobe and two negative lobes as shown in Figure 7. We can write

$$s_i = \int H_i(\hat{x})T(\hat{x})dx. \quad (8)$$

We will consider this a single measurement at a pixel  $\hat{x}$ . In practice, we make a set of  $N$  similar measurements over a patch of sky. For a first order estimate, we may find the intrinsic variance of the sky from

$$\sigma_{sky}^2 = \sigma_{meas}^2 - \sigma_{data}^2, \quad (9)$$

where  $\sigma_{data}^2$  is the square of the average statistical error per measurement and  $\sigma_{meas}$  is the variance of the  $N$  data points. This answer is usually only correct to 25% so it is used as a sanity check. Also, it does not give the correct error. Note too that this method ignores all intrinsic correlations in the data.

What variance does one expect from such a measurement? After working through the math, we find that the inclusion of finite beams modifies eq. 3 to the following:

$$C_T^{ij} = \sum_L \frac{2l+1}{4\pi} C_l W_l^{ij}, \quad \text{where } W_l^{ij} = \int dx_1 \int dx_2 H_i(\hat{x}_1) H_j(\hat{x}_2) P_l(\hat{x}_1 \cdot \hat{x}_2). \quad (10)$$

This is the full theoretical covariance matrix for the observing pattern for measurements  $i$  and  $j$ .<sup>7</sup>  $W_l$  is called the window function, it tells us the portion of  $l$ -space being examined. Generally, just the diagonal elements are plotted. For the beam in Figure 7, the window function is shown in Figure 8. When  $i = j$ , we get a prediction for  $\sigma_{sky}^2$ .

The most frequently used analyses follow Bond’s work [4]. A complete analysis requires knowledge of the covariance matrix of the data; we call this  $C_D$ . The full theory-plus-data covariance matrix is given by  $M = C_D + C_T$ . Our goal is to determine the probability of a theory given the data,  $P(T|D)$ . To do this, we use Bayes’s theorem with a uniform prior,  $P(T) = 1$ , and set the probability of getting the data,  $P(D)$ , equal to 1:

<sup>7</sup>From a theoretical perspective, our universe is one realization of a cosmological model that can only predict the ensemble average of  $C_l$ . Even if we knew the correct physics, the data would be scattered around the predicted  $C_l$  with a “cosmic variance.”



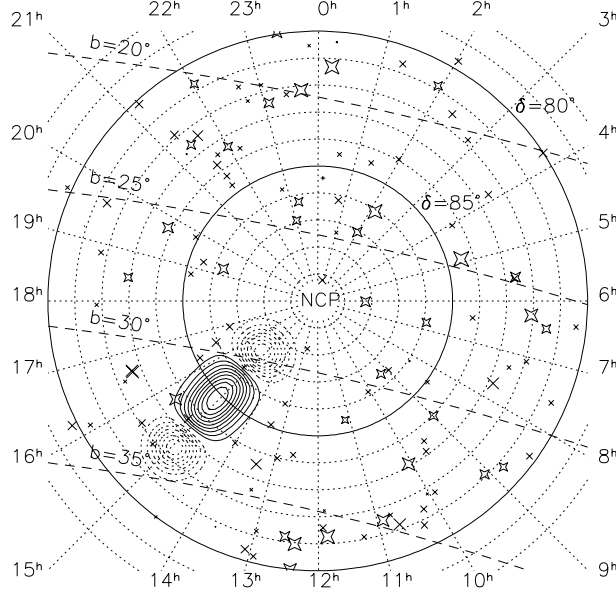


**Figure 7.** Contour plot of a typical double-difference beam superimposed on a source map of the north celestial polar region from Netterfield *et al.* [54]. This profile corresponds to  $H_i(\hat{x})$  in eq. 8. The dashed lines are negative and the solid lines are positive. The sources come from the Kühr survey[55]. The stars mark the flat spectrum sources. The symbol size is proportional to the log of the flux. Lines of Galactic latitude are also shown.

$$P(T|D) = \frac{P(D|T)P(T)}{P(D)} = L(D|T) = \frac{\exp(-t^T M^{-1}t/2)}{(2\pi)^{N/2}|M|^{1/2}}, \quad (11)$$

where  $L$  is the likelihood function and  $t$  is a vector of the data. The argument of the exponent is proportional to  $\chi^2$ . This boils down to saying that the likelihood of the data plotted as a function of some parametrization, for instance  $\sigma_{sky}$ , is the probability of obtaining  $\sigma_{sky}$  with a given set of data. When the signal to noise is high, the likelihood is fairly Gaussian. To get an error, we find bounds symmetric around the maximum, that contain 68% of the area under the likelihood curve.

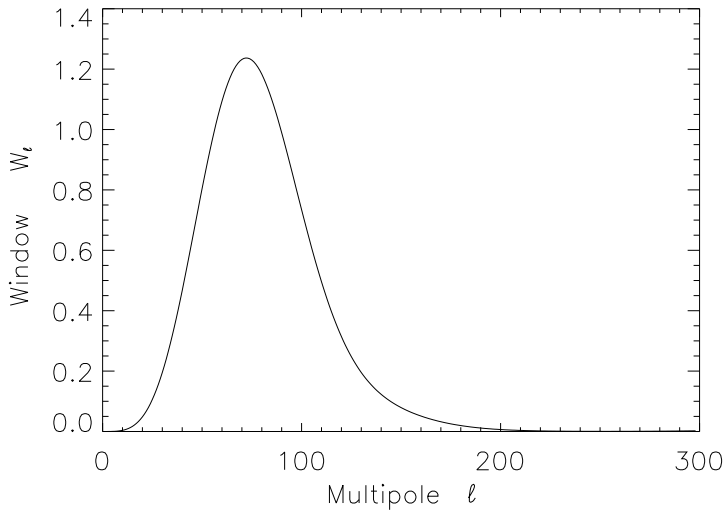


**Figure 8.** Window function for the beam in Figure 7 using eq. 10 with  $i = j$ . The amplitude of the window depends on the normalization of the beam. For this plot,  $\int d\hat{x}|H(\hat{x})| = 2$  was used.

To estimate the angular spectrum, we take the most likely value of  $\sigma_{sky}$  with its error, convert it into a “band-temperature”<sup>8</sup> and plot it at the  $l$ -weighted center of the window function. A horizontal error bar is often plotted indicating the width of the window function. Any one experiment observes in multiple windows and so the spectrum may be mapped out. One example is given in Figure 9 from the Saskatoon experiment [18].

## 6. Anisotropy Measurements: The Current Results and Immediate Future

The anisotropy of the CMB was first unambiguously measured by the DMR experiment aboard the *COBE* satellite [57] using  $7^\circ$  resolution full-sky maps at 30, 53, and 90 GHz. To date, these are still the cleanest and best checked data. All indications are that the fluctuations are thermal, though I am not aware of any formal limits on, say, the Compton  $y$  parameter of the anisotropy. When smoothed to a  $10^\circ$  resolution, the *rms* of the temperature fluctuations is about  $30 \mu\text{K}$ . This is the canonically quoted value. However,

<sup>8</sup>See Bond [56] for details. One obtains a band power by dividing  $\sigma_{sky}$  by  $\sqrt{\sum_l W_l/l}$ . This makes sense because  $\sigma_{sky} = \sqrt{\sum (\delta T_l)^2 W_l/l}$  can be written as  $\sigma_{sky} = \delta \bar{T}_l \sqrt{\sum W_l/l}$ .

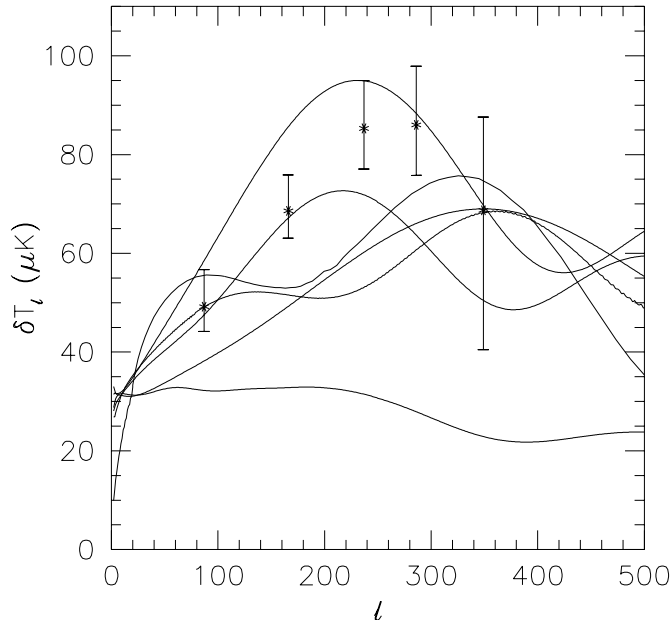


**Figure 9.** Results from the Saskatoon experiment [71], [18]. The spectra from six theories are also shown. From top to bottom at  $l = 160$  they are a flat  $\Lambda$ +CDM model with  $\Omega_\Lambda = 0.7$  [38], Standard CDM [19], a PPI model [62], an  $\Omega_0 = 0.4$  open bubble model [19], a texture model [63], and a model with reionization [64]. There is a 14% overall calibration uncertainty that is not included in the error bars. This affects the normalization of the spectrum, but not the shape.

with a  $1/2^\circ$  resolution map, the *rms* is closer to  $90 \mu\text{K}$ . The final DMR results (the satellite is now turned off) are published in Ap.J Vol 464, 1996 [58], [17], [59], [60], & [61]. The lasting contribution will be the maps of the sky at 30, 53, and 90 GHz. A combination of these maps, optimized to give the anisotropy, has a signal-to-noise of two per  $10^\circ \times 10^\circ$  pixel. The two primary results derived from these maps are:

1. From a fit of the data to a power spectrum parameterized by the spatial index and the quadrupole amplitude, the DMR team finds  $n_{DMR} = 1.21 \pm 0.3$  and  $Q_{rms-PS} = 15.3^{+3.8}_{-2.8} \mu\text{K}$ . The quadrupole of the raw maps is slightly below  $Q_{rms-PS}$ , but not by a statistically significant amount. Note that for “standard CDM” one expects  $n_{DMR} = 1.1$  because DMR probes the low- $l$  tail of the acoustic peak.

In this notation, the  $C_l$  (eq. 10) are given by [66]:

$$C_l = \frac{4\pi}{5} Q_{rms-PS}^2 \frac{\Gamma[l + (n_{DMR} - 1)/2] \Gamma[(9 - n_{DMR})/2]}{\Gamma[l + (5 - n_{DMR})/2] \Gamma[(3 + n_{DMR})/2]} \quad (12)$$

with  $n_{DMR} = 1$  this reduces to  $C_l \propto 1/l(l+1)$ .

2. The data appear best described by Gaussian statistics [65]. At these large angular scales this is not surprising because even non-Gaussian processes at small scales, when averaged over a large enough volume, appear Gaussian. However, it is reassuring that the statistics we all assume have some basis in reality.

My favorite way of quantifying the DMR maps is to show the power spectrum over compact regions of  $l$ -space. A direct computation of the power spectrum is hampered by the unevenly-weighted non-uniform sky coverage imposed by the scan pattern and the elimination of data contaminated by Galactic emission. There are a number of ways around this problem ([69], [70]). The most recent approaches ([68], [67]) work to minimize the width of a representative bin in  $l$ -space. The results are shown in Figure 10. Górski's method in particular shows the power within  $\Delta l = 0$ . Though one should expect to get exactly the same results from two different methods applied to the same data set, we can be pleased by the general concordance.

Many groups are working to measure the anisotropy. Though some are focussing on large angular scales and frequencies not observed with DMR, most concentrate on smaller angular scales. Table 1 contains a list for recent, current and planned experiments. It does not include the satellite experiments nor does it claim to be comprehensive. I apologize for any omissions or misrepresentations.

Unlike measurements of the absolute temperature of the CMB, where the final result is completely dominated by one's control of subtle systematic errors, anisotropy measurements require a combination of high sensitivity and immunity to systematic effects. The state-of-the-art in absolute measurements, excluding FIRAS, is 1% [30]; the anisotropy has yet to be measured to 15% accuracy.

To give a broad and almost un-biased sense of what the anisotropy data are telling us, we take the compilation from Ratra [97] (which I believe is the most comprehensive and thoroughly checked compilation to date) and bin the data according to the following:

- Select logarithmically spaced bins in  $l$  with four bins per decade.
- Ignore the widths of window functions and add data to a bin according to the value of the weighted mean of the window,  $l_e$  in [97]. Many of the data have  $\Delta l/l_e < 1/4$  so this is not the bin it may at first appear.

TABLE 1. Recently Completed, Current and Planned Anisotropy Experiments

Experiment	Resolution	Frequency	Detectors	Type	Groups
ACE(c)[72]	0.2°	25-100 GHz	HEMT	C/B	UCSB
APACHE(c)[73]	0.33°	90-400 GHz	Bol	C/G	Bologna, Bartol Rome III
ARGO(f)[74]	0.9°	140-3000 GHz	Bol	C/B	Rome I
ATCA[75]	0.03°	8.7 GHz	HEMT	I/G	CSIRO
BAM(c)[76]	0.75°	90-300 GHz	Bol	C/B	UBC, CfA
Bartol(c)[77]	2.4°	90-270 GHz	Bol	C/G	Bartol
BEAST(p)[72]	0.2°	25-100 GHz	HEMT	C/B	UCSB
BOOMERanG(p)[78]	0.2°	90-400 GHz	Bol	C/G	Rome I, Caltech UCB, UCSB
CAT(c)[53]	0.17°	15 GHz	HEMT	I/G	Cambridge
CBI(p)[79]	0.0833°	26-36 GHz	HEMT	I/G	Caltech, Penn.
FIRS(f)[47]	3.8°	170-680 GHz	Bol	C/B	Chicago, MIT, Princeton, NASA/GSFC
HACME/SP(f)[80]	0.6°	30 GHz	HEMT	C/G	UCSB
IAB(f)[81]	0.83°	150 GHz	Bol	C/G	Bartol
MAT(p)[82]	0.2°	30-150 GHz	HEMT/SIS	C/G	Penn, Princeton
MAX(f)[83]	0.5°	90-420 GHz	Bol	C/B	UCB, UCSB
MAXIMA(p)[84]	0.2°	90-420 GHz	Bol	C/B	UCB, Caltech
MSAM(c)[85]	0.4°	40-680 GHz	Bol	C/B	Chicago, Brown, Princeton, NASA/GSFC
OVRO 40/5(c)[86]	0.033°, 0.12°	15-35 GHz	HEMT	C/G	Caltech, Penn
PYTHON(c)[87]	0.75°	35-90 GHz	Bol/HEMT	C/G	Carnegie Mellon Chicago, UCSB
QMAP(f)[88]	0.2°	20-150 GHz	HEMT/SIS	C/B	Princeton, Penn
SASK(f)[89]	0.5°	20-45 GHz	HEMT	C/G	Princeton
SuZIE(c)[90]	0.017°	150-300 GHz	Bol	C/G	Caltech
TopHat(p)[91]	0.33°	150-700 GHz	Bol	C/B	Bartol, Brown, DSRI, Chicago, NASA/GSFC
Tenerife(c)[92]	6.0°	10-33 GHz	HEMT	C/G	NRAL, Cambridge
VCA(p)[93]	0.33°	30 GHz	HEMT	I/G	Chicago
VLA(c)[94]	0.0028°	8.4 GHz	HEMT	I/G	Haverford, NRAO
VSA(p)[95]	–	30 GHz	HEMT	I/G	Cambridge
White Dish(f)[96]	0.2°	90 GHz	Bol	C/G	Carnegie Mellon

1. For “Type” the first letter distinguishes between configuration or interferometer, the second between ground or balloon.
2. An “f” after the experiment’s name means it’s finished; a “c” denotes current; a “p” denotes planned, building may be in progress but there is no data yet.

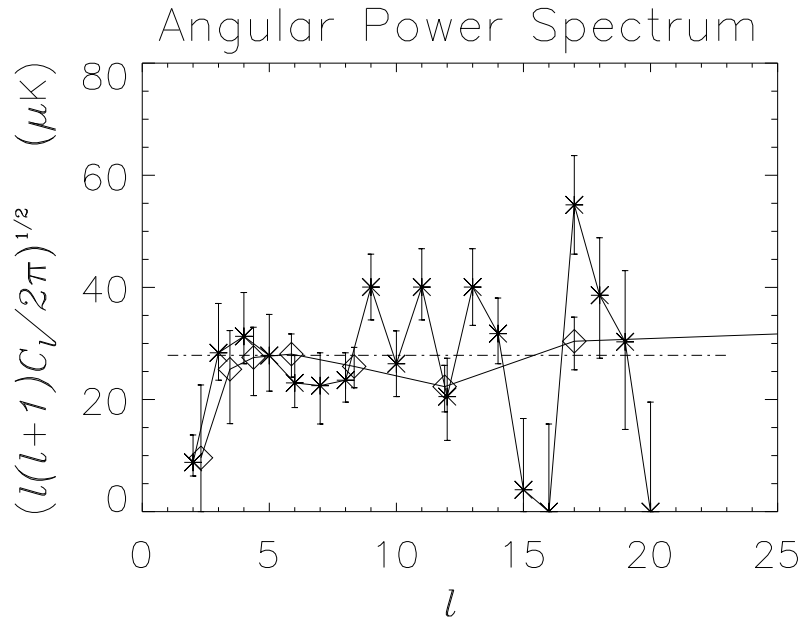


**Figure 10.** The angular power spectrum from DMR. Results from Górski [67] (stars) and Tegmark [68] (diamonds) are shown. Both have analyzed the data in a manner to produce narrow window functions. Górski's, in particular, have  $\Delta l/l = 0$ . One should bear in mind that Górski's results are derived from non-Gaussian likelihood distributions. The flat dashed line is for a Harrison-Zel'dovich spectrum with  $Q_{rms-PS} = 18 \mu\text{K}$ .

- Compute the weighted mean of the data that fall into each bin and call that the band-power  $\delta\bar{T}$ . Use the inverse root of the total weight as the error bar. Use all the *unique* data in [97]. Be aware that many of the data points are unconfirmed!
- Compute the arithmetic mean value  $\bar{l}$ , of the  $l_e$  that fall in a given bin.
- Plot  $\bar{l}$  versus  $\delta\bar{T}$  and connect the ends of the error bars.
- Ignore the intrinsic calibration uncertainties and the relative calibration uncertainties.
- Ignore upper limits for  $l < 500$ . For some cases, (eg SASK[89]), the data can be combined to give a detection [18].
- In addition to the Ratra compilation, add the Tegmark results [68], ATCA [75], and the new CAT [53] results.

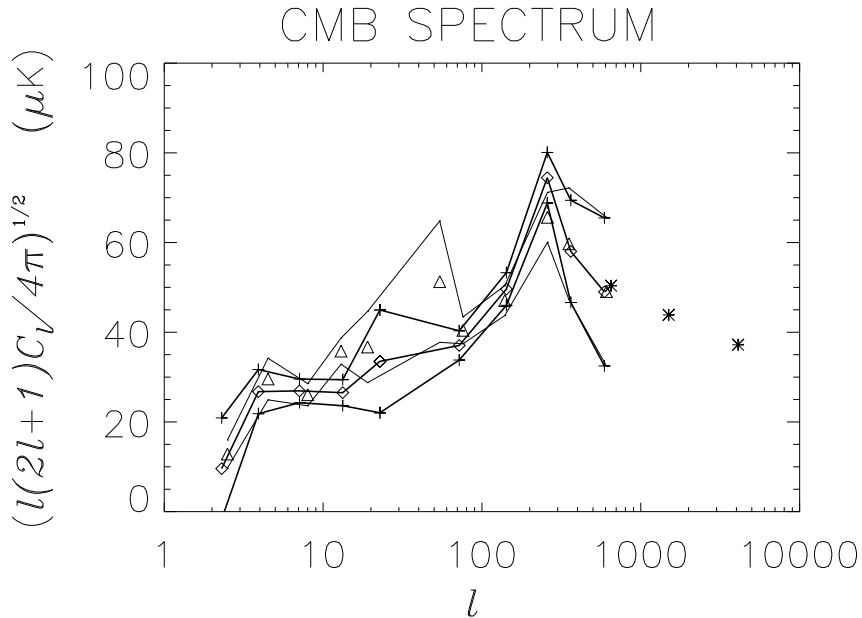


**Figure 11.** Angular spectrum of the anisotropy. The thick lines (diamonds) were obtained following the prescription given in the text. Bharat Ratra has used somewhat different criteria and obtained the results indicated by the thin lines. The asterisks near  $l = 1000$  are upper limits. Clearly, the data indicate a rise in the spectrum from  $l = 10$  to  $l \approx 200$ . For  $l > 20$ , the quantity on the y-axis is the same as in Figure 3.

The principle conclusion one should draw from Figure 11 is that there is a general rise in  $\delta T_l$  as one moves from the *COBE* scales to smaller angular scales. This is a stunning observation that was predicted long before the anisotropy was discovered. Has a peak to the spectrum been detected? Possibly, but it is still too early to say this with any confidence. All indications are that the power spectrum at  $l \approx 10$  is lower than at  $l \approx 200$  but we cannot say where the spectrum turns over above  $l \approx 200$ . The errors are simply too large and there are too many systematic effects hidden in the data. Also, there are plenty of examples where 95% upper limits have become detections at a higher level and examples where detections have become upper limits. However, it is somewhat reassuring that the  $\chi^2/(\nu - 1)$  for most of the individual bins is not too different from one.

The measurements have come a long way in the past two years. In three cases multiple experiments have observed the same region of sky and seen the same thing. They are DMR and FIRS [98], DMR and Tenerife[92], and MSAM ([99], [100] & [101]) and SASK [18], [8]. The spectrum of the fluctuations for MSAM and SASK is thermal from 25 to 200 GHz. However, one should still view the data with some caution. In the analyses that give rise to Figure 11, an entire data set is reduced to give one measurement and one statistical error bar. When this is done, there is simply not enough signal-to-noise to quantify systematic effects that are lurking at the  $1\sigma$  to  $2\sigma$  level. On top of this, the analysis of these experiments is tricky; “new” effects are still being discovered by many groups. Finally, the inter-calibration of the experiments is uncertain to the 10%-15% level.

To improve on these results, a number of experimental and observational challenges must be met. The results that went into Figure 11 are primarily from difference measurements. Eventually we will want maps of the sky so that experiments are easily compared, foreground contamination is more easily identified, and powerful statistical tests can be performed. Interferometers offer one proven way to do this at low frequencies (and eventually at higher frequencies) but other techniques and strategies are needed. The calibration of the experiments must be better than 10% in order to distinguish between the various models. Currently, the best reference is the intrinsic dipole in the CMB. Finally, to distinguish features near  $l \approx 1000$ , high resolution will be needed. One desires at least  $\delta l/l \approx 1/10$ . Lower resolutions smear the features in the power spectrum.

A measurement of the polarization in the CMB is now within grasp. In the standard CDM models, the signal is predicted to be at 1% to 5% of the anisotropy[66]. John Ruhl at Santa Barbara, Suzanne Staggs at Princeton, and Peter Timbie at Wisconsin are actively working on these measurements. The polarization is caused by Thompson scattering. At angular scales of order ten degrees, the polarization may be used to identify any primordial gravity waves (tensor modes) though the signal is expected to be largest at degree scales. Crittenden and Turok [102] point out that there is a correlation between the polarization and the anisotropy that is different for the scalar and tensor modes. This correlation should also aid in separating the CMB polarization from polarized foreground emission, about which very little is known.

## 7. The New Satellite Experiments

Two satellite missions are planned that will endeavor to map the CMB anisotropy over the entire sky. The ESA mission is called *PLANCK* (originally *COBRAS/SAMBA*). The NASA mission, which is in the final design



and definition phase, is called *MAP*. Because I am part of the *MAP* team, I will focus on it.

*PLANCK*<sup>9</sup> uses both bolometers and HEMT- based amplifiers. It will carry cryogenics so that the bolometers may be operated at 0.1 K. At this stage in the design, the instrument is planned to span the frequencies between roughly 30 and 900 GHz with an angular resolution between 30' and 4.4'. The lower frequency channels will be polarization-sensitive. The planned launch date is 2005.

*MAP* is based on the HEMT amplifiers developed by Marian Pospieszalski. The radiometers are intrinsically polarization-sensitive and differential, similar in some regards to the successful *COBE*/DMR design. The instrument will span from 20 to 106 GHz in five frequency bands with an angular resolution ranging between 54' and 15'. The sensitivity per  $0.3^\circ \times 0.3^\circ$  pixel (of which there are roughly 400,000 in the sky) will be about 35  $\mu$ K. Because the instrument is passively cooled, it can in principle observe longer than the 15 month design life.

The primary goal of *MAP* is to make multi-frequency, high-fidelity, high-sensitivity maps of the sky. This requires extreme control of systematic effects. We believe the best vantage for these observations is L2, the Earth-Sun Lagrange point. At L2, the Sun, Earth, and moon are  $\approx 90^\circ$  out of the beams and the environment is essentially isothermal. From the work on DMR and balloons, the team has found that successful map production requires reference of one pixel to another over many directions and over many time scales. *MAP* plans to do this with the scan strategy shown in Figure 12.

From a high-quality map, one may not only obtain the power spectrum, but may also compare the data to the results of other CMB experiments and to maps of the foreground emission at different frequencies. Also, a map gives the best data set for testing the underlying statistics of the fluctuations. For instance, we will be able to tell from the *MAP* data if the CMB is a Gaussian random field. Finally, with its high sensitivity and large scale coverage, the time-line data from *MAP* will be ideal for searching for transient radio emission.

The question of how well one can determine the parameters of cosmological models is still an active area of research. The most recent published work on parameter estimation for inflation-based models is in [36] but one must remember that there are other classes of promising models. At this school, Dick Bond discussed an approach where one works in an eigen-parameter space to circumvent the strong covariance between many of the standard parameters such as  $\Omega_B$ ,  $\Lambda$ ,  $h$ , etc. At any rate, if the anisotropy is

<sup>9</sup>See web site <http://astro.estec.esa.nl/sa-general/projects/cobras/cobras.html> for additional information.

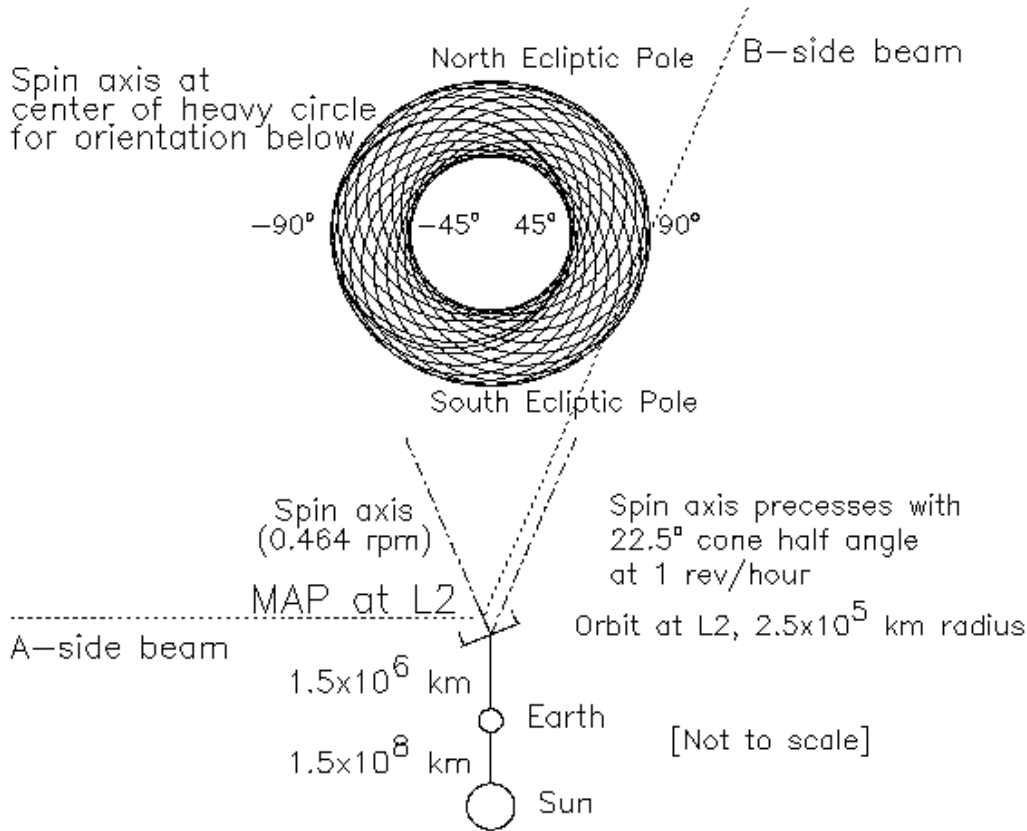


**Figure 12.** The *MAP* scan pattern for one hour of observation. The lines show the path for one side of a differential pair. The other pair member follows a similar path, only delayed by 1.1 min. There are four principal time scales for the observations. The phase of the difference signal is switched by  $180^\circ$  at 2.5 KHz. The spacecraft spins around its symmetry axis with a 2.2 min period (bold circle) with cone opening angle of roughly  $135^\circ$ . This pattern precesses about the Earth-Sun line with a period of 60 minutes. Thus, in about 1 hour, over 30% of the sky is covered. Every six months, the whole sky is observed. Note that any pixel is differenced to another pixel in many directions.

normally distributed, the *MAP* CMB data will be cosmic variance limited up to  $l \approx 600$  (assuming the foreground/radio source emission is successfully removed) and will probe multipoles up to  $l \approx 1000$ .

In the current schedule, the satellite design and definition will be com-

plete by November 1997 and then the building will begin. *MAP* is scheduled for launch late in 2000. The *MAP* science team is comprised of Chuck Bennett (PI) at NASA/GSFC, Mark Halpern at UBC, Gary Hinshaw at NASA/GSFC, Norm Jarosik at Princeton, John Mather at NASA/GSFC, Steve Meyer at Chicago, Lyman Page at Princeton, Dave Spergel at Princeton, Dave Wilkinson at Princeton, and Ned Wright at UCLA. More information about *MAP*, the CMB, and other experiments may be obtained from <http://map.gsfc.nasa.gov/>.

I would like to thank Roberta Bernstein, Venya Berezhinsky, Piero Galletti, David Schramm and the Ettore Majorana Center staff for organizing a wonderful school. Marsala will never taste the same. Conversations with many colleagues were helpful in preparing these notes. I would especially like to thank Tom Herbig, Gary Hinshaw, Bharat Ratra, Suzanne Staggs, and Ned Wright. Ned gave me the computer code to produce Figure 4. This work was supported by the US National Science Foundation and the David and Lucile Packard Foundation.

## References

1. Weiss, R., *Ann. Rev. Astron. Astrophys.*, 1980, 18:489.
2. Readhead, A. C. S. and Lawrence, C. R., *Ann. Rev. Astron. Astrophys.*, 1992, 30:653.
3. White, M. Scott, D. and Silk, J. *Ann. Rev. Astron. Astrophys.*, 1994, 32:319.
4. Bond, J. R., in *Cosmology and Large Scale Structure*, ed R. Schaeffer, 1995, Elsevier Science Publishers, Netherlands
5. Tegmark, M. Proc. Enrico Fermi Course CXXXII, Varenna, 1995. (astro-ph/9511079)
6. Hu, W., Sugiyama, N. & Silk, J. Review for Nature, 1996, (astro-ph/9604166).
7. Smoot, G. & Scott, D. Current Summary of Results. in L. Montanet et al. *Phy. Rev D*50, 1173 (1994), off-year addition (astro-ph/9603157).
8. Page, L., Proceedings from the Critical Dialogues in Cosmology Conference, Princeton NY, June 1996.
9. Sunyaev, R. A. & Zel'dovich, Ya. B. *Ann. Rev. Astron. Astrophys.*, 1980, 18:537.
10. Danese, L., Burigana, C. Toffolatti, L., De Zotti, G. & Franceschini, A. *The Cosmic Microwave Background: 25 Years Later*, 153, 1990, Kluwer Academic Publishers. Mandolesi & Vittorio (eds.)
11. Bartlett, J. G., Stebbins, A. 1991, *ApJ*, 371:8.
12. Partridge, B. "3K: The Cosmic Microwave Background Radiation", Cambridge University Press, 1995.
13. Wright, E. L. et al., 1991, *Ap.J.* 381:200.
14. *COBE* is the COsmic Background Explorer. The three experiments aboard the satellite are the Differential Microwave Radiometers (30-90 GHz, DMR), the Far-InfraRed Absolute Spectrophotometer (60-630 GHz, FIRAS), and the Diffuse InfraRed Background Experiment (1.2-240  $\mu\text{m}$ , DIRBE) All the experiments produce maps of the sky.
15. Haslam et al., 1982 *A&AS*, 47, 1 1991b, *ApJ*, 379, 1
16. Available through the Infrared Processing and Analysis Center in Pasadena, CA.
17. Kogut, A. et al. 1996, *Ap.J.* 464:L5-L9.
18. Netterfield, C. B. et al., 1997, *ApJ.* accepted, (astro-ph/9601197).
19. Ratra, B. Banday, A. J., Górski, K. M., & Sugiyama, N. 1995, (astro-ph/9512145).
20. Tegmark, M. and Efstathiou, G. Submitted to *MNRAS* (astro-ph/9507009).

21. Mather, J. C., et al. 1994, Ap. J. ApJ, 420:439.
22. Fixsen, D. J., et al. 1996, ApJ, 473:576. (astro-ph/9605054).
23. Fixsen, D. J., et al. 1994, ApJ, 420:457
24. Gush, H. et al., 1990, PRL, 65, 537.
25. Private communication, June 1996.
26. Rybicki and Lightman. "Radiative Processes in Astrophysics" John Wiley& Sons, New York, 1979.
27. Wright, E. L., et al. 1994, Ap. J. ApJ, 420:450.
28. Bersanelli, M. et al., 1994, Ap.J. 424:517.
29. Peebles, P. J. E. et al. 1991, Nature, 352:769.
30. Staggs, S. T., et al, 1996, ApJ 473:L1 (astro-ph/9609128).
31. The team of R. Shafer, M. Mather, M. DiPirro, A. Kogut, D. Fixsen, M. Seiffert, P. Lubin, & S. Levin have designed a satellite mission called DIMES (Diffuse Microwave Emission Survey) to measure the CMB temperature between 2 and 100 GHz to 0.1 mK accuracy. A subset of this team is also building a balloon experiment for a multi-frequency absolute measurement. They hope to fly in early 1997. More information may be obtained from <http://ceylon.gsfc.nasa.gov/DIMES/>
32. Burigana, C., Danese, L.& De Zotti, G.F. 1991a, A&A, 246, 49
33. Burigana, C., Danese, L.& De Zotti, G.F. 1991b, ApJ, 379, 1
34. Smith, C., 1996, Ph.D. Thesis, Princeton University.
35. Staggs, S., 1993, Ph.D. Thesis, Princeton University.
36. Jungman, G., Kamionkowski, M., Kosowsky, A. and Spergel, D. Phys. Rev. D, 1996, 54 1332.
37. Peebles, P. J. E., 1994, ApJ 419:L49.
38. Ratra, B. & Sugiyama, N. 1995, (astro-ph/9512157)
39. Silk., J. 1968, ApJ, 151:459.
40. Sunayev, R.A. and Zel'dovich Y. B., 1970, Astrophysics and Space Science, 7:3-19, Reidel, Dordrecht-Holland.
41. Peebles P.J.E. and Yu ,J.T., 1970, AP.J 162:815.
42. Hu, W. and White, M. 1996, IAS preprint IASSNS-AST 96/47. Submitted to Ap.J. Available through <http://www.sns.ias.edu/whu>.
43. Kanionkowski, M., Spergel, D. N., & Sugiyama, N. 1994, ApJ, 426:L57.
44. Timbie, P, 1985, Ph.D. Thesis, "A Novel Interferometer to Search for Anisotropy in the 2.7 K Background Radiation." Princeton.
45. Meinhold, P., 1989 Ph.D. Thesis, "Anisotropy Measurements of the Cosmic Microwave Background Radiation at 3 mm Wavelength and an Angular Scale of 30 Arcminutes." UCB
46. Robertson, T. 1996, Senior Thesis, Princeton University.
47. FIRS. The Far InfraRed Survey. This is an experiment that started at MIT but has since moved to Princeton, University of Chicago and NASA/GSFC. It is a bolometer-based balloon-borne radiometer. It confirmed the initial COBE/DMR discovery.
48. Bock, J. et al. Proceedings of "Submillimeter and Far-Infrared Space Instrumentation," 30<sup>th</sup> ESLAB Symposium, 24-26 Sept. 1996, ESTEC, Noordwijk, The Netherlands.
49. Kowitt, M. S. et al. 1996, Appl. Opt. 35:5630.
50. Nahum, M. & Martinis, J. M. 1993, "Novel Hot-electron Bolometer" Proceedings from 20<sup>th</sup> conference on Low-Temperature Physics, Eugene, OR.
51. Downey, P. M. et al. 1984, Appl. Opt. 239:10
52. Lee, A. T. et al. 1996, Preprint, To appear in Appl. Phys. Lett.
53. CAT. This is the Cambridge Anisotropy Telescope. It operates near 15 GHz and produces images of the microwave background. Early results are reported in Scott et al. 1996, Ap.J. 461:L1.
54. Netterfield, B et al., 1995 ApJ 445:L69
55. Kuhr, H. Pauliny-Toth, I.I.K., Witzel, A. & Schmidt, J. 1981, AJ, 86, 854.
56. Bond, J. R., Astro. Lett. & Comm. Vol 32, No. 1, 1995. Presented in 1994.

57. Smoot, G. F. et al. 1992, Ap.J. 396:L1.
58. Bennett, C. et al. 1996, Ap.J. 464:L1-L4.
59. Górski K. et al. 1996, Ap.J. 464:L11-L15.
60. Hinshaw G. et al. 1996, Ap.J. 464:L17-L20.
61. Wright E. et al. 1996 Ap.J. 464:L21-L24.
62. Peebles, P.J.E. 1995, Private Communication
63. Crittenden, R. G. & Turok, N. 1995, PRL, 75, 14
64. Sugiyama, N. 1995, Ap.J., 100, 281
65. Kogut, A. et al., 1996, ApJ 464:L29-L33.
66. Bond, J. R. & Efstathiou, G. 1987, MNRAS, 226, 655.
67. Górski, K. M. 1996, Private Communication
68. Tegmark M. 1996, Ap.J. 464:L35.
69. Hauser, M. G. & Peebles, P.J.E., 1973, Ap.J. 185:757.
70. Górski, K. M. 1994, Ap.J. 430:L85.
71. Wollack E. et al. 1997, ApJ, Accepted (astro-ph/9601196).
72. ACE and BEAST. These two new projects are aimed at using HEMTs between 26 and 100 GHz on both super-pressure and conventional long-duration balloon platforms. The finest angular resolution will be near  $1/5^\circ$ .
73. APACHE. This experiment will observe from Dome-C in the Antarctic. Web site <http://tonno.tesre.bo.cnr.it/valenzia/APACHE/apache.html> contains more information.
74. ARGO. A balloon-borne bolometer based experiment. Results are reported in de Bernardis, et al. 1994, Ap.J. 422:L33.
75. ATCA: Australia Telescope Compact Array. An interferometer operating at 8.7 GHz with a  $2'$  resolution produced a map that was analyzed for anisotropy. The results are reported in Subrahmanyam R., Ekers, R. D., Sinclair, M. & Silk, J. 1993, MNRAS 263:416.
76. BAM: Balloon Anisotropy Measurement. This uses a differential Fourier transform spectrometer to measure the spectrum of the anisotropy between 90 and 300 GHz. Recent results are reported in astro-ph/9609108. More information may be obtained from <http://cmb.physics.ubc.edu>.
77. Bartol. This is a bolometer-based experiment designed to look at  $2^\circ$  angular scales. It observed from the Canary Islands. Results are reported in Piccirillo et al., astro-ph/9609186.
78. BOOMERanG is a collaboration between the Caltech, Berkeley, Santa Barbara (Ruhl) and Rome groups. It will use bolometers to measure the anisotropy in the CMB between 90 and 410 GHz. The ultimate goal is a circumpolar Antarctic flight.
79. CBI: Cosmic Background Imager. This is an interferometer that plans to produce maps of the microwave sky near 30 GHz.
80. HACME/SP. This uses HEMTs on the ACME telescope. Observations were made from the South Pole. Recent results are reported in Gundersen, J. et al. 1995, Ap.J. 443:L57.
81. IAB. A bolometer-based experiment carried out at the Italian Antarctic Base. Results are reported in Piccirillo, L. & Calisse, P. 1993, Ap.J. 413:529.
82. MAT. This is the Mobile Anisotropy Telescope. It is similar to QMAP but is designed to operate from the ground in Chile.
83. MAX was a collaboration between UCSB and Berkeley. It is a balloon-borne bolometer-based radiometer spanning roughly between 90 and 420 GHz. Recent results are reported in Lim et al. 1996, Ap. J. 469:L69. It flew on the ACME telescope.
84. MAXIMA is a collaboration between Caltech and Berkeley. It is the next generation of MAX. Web site <http://physics7.berkeley.edu/group/cmb/gen.html> contains more information.
85. MSAM. There are a number of versions of MSAM. All use bolometers of various sorts and fly on balloons. The MSAM collaboration includes NASA/GSFC, Bartol Research Institute, Brown University, and the University of Chicago.

86. OVRO. The Owen's Valley Radio Observatoty telescopes operate with various receivers between 15 and 30 GHz. The 40 m dish has a 2' beam, and the 5.5 m has a 7.3' beam. The experiments are aimed primarily at small angular scales.
87. PYTHON. A multi-pixel bolometer- and HEMT- based experiment operated from the ground at the South Pole. The experiment has run in a number of configurations. Recent results are reported in Ruhl, J., et al. 1995, Ap.J., 453:L1.
88. QMAP. This is a balloon-borne experiment that uses a combination of HEMTs and SIS detectors. The angular resolution is  $1/5^\circ$ . This experiment is designed to produce "true" maps of the sky.
89. SASK. These experiments are based on HEMT amplifiers operating between 26 and 46 GHz. They were performed in Saskatoon, Saskatchewan CA. Three years of observations have gone into the final data set.
90. SuZIE is a bolometer-based experiment that observes from the ground. It is primarily intended to measure the SZ effect at high frequencies though it will also give information on the anisotropy at small scales.
91. TopHat is a collaboration between Bartol Research Institute, Brown University, DSRI, NASA/GSFC, and the University of Chicago. The group plans to observe with an extremely light-weight bolometer-based payload mounted on top of a scientific balloon that circumnavigates the Antarctic. For more information see <http://cobi.gsfc.nasa.gov/msam-tophat.html>.
92. Tenerife. Ground-based differential radiometers with 10-33 GHz receivers. The resolution is about  $6^\circ$ . The experiment observes from the Observatorio del Teide in Tenerife, Spain. It has operated for many years. Recent results are discussed in Hancock et al. 1994, Nature, 367, 333.
93. VCA: Very Compact Array. This is an interferometer being developed at the University of Chicago. It will produce maps of the CMB at 30 GHz and be sensitive to larger angular scales than CBI.
94. VLA. This is work done near 5 GHz, on arcminute and smaller angular scales. It uses the Very Large Array. Recent results are reported in Fomalont et al. 1993, Ap.J. 404:8-20.
95. VSA: Very Small Array. This is a 30 GHz interferometer; the next generation of CAT. Web site <http://www.mrao.com.ac.uk/telescopes/cat/vsa.html> contains more information.
96. White Dish. This experiment uses an on-axis Cassegrain telescope and a 90 GHz single-mode bolometer. It observed at the South Pole and is sensitive to small angular scales. Results are reported in Tucker et al., 1993, Ap.J. 419:L45.
97. Ratra, B. 1996. The original compilation was reported in Ratra & Sugiyama, 1995. This is available through astro-ph/9512157. Ratra has kept the list up-to-date and kindly supplied his more recent results.
98. Ganga, K. M. et al. 1993, Ap.J. 432:L15-L18.
99. Cheng, E. S. et al., 1994, Ap.J. 422:L37-L40.
100. Cheng, E. S. et al., 1996, Ap.J. 456:L71-L74.
101. Inman, C. A. et al, Submitted to Ap.J. Letters; astro-ph/9603017.
102. Crittenden, R. G., Coulson D., & Turok, Phys. Rev. D, 1995, D52, 5402. See also astro-ph/9408001 and astro-ph/9406046.